JOURNAL OF THE AMERICAN CHEMICAL SOCIETY
pubs.acs.org/JACS
Article

Gold-Cage Perovskites: A Three-Dimensional Au^{III}−X Framework Encasing Isolated MX_6^{3-} Octahedra (M^{III} = In, Sb, Bi; X = Cl^-, Br^-, I^-)

Kurt P. Lindquist,[\$] Michael A. Boles,[\$] Stephanie A. Mack, Jeffrey B. Neaton,
and Hemamala I. Karunadasa*

Cite This: *J. Am. Chem. Soc.* 2021, 143, 7440−7448
Read Online

ACCESS | Metrics & More | Article Recommendations | Supporting Information

ABSTRACT: The $Cs_8Au^{III}_4M^{III}X_{23}$ (M = In^{3+}, Sb^{3+}, Bi^{3+}; X = Cl^-, Br^-, I^-) perovskites are composed of corner-sharing Au−X octahedra that trace the edges of a cube containing an isolated M−X octahedron at its body center. This structure, unique within the halide perovskite family, may be derived from the doubled cubic perovskite unit cell by removing the metals at the cube faces. To our knowledge, these are the only halide perovskites where the octahedral sites do not bear an average 2+ charge. Charge compensation in these materials requires a stoichiometric halide vacancy, which is disordered around the Au atom at the unit-cell corner and orders when the crystallization is slowed. Using X-ray crystallography, X-ray absorption spectroscopy, and pair distribution function analysis, we elucidate the structure of this unusual perovskite. Metal-site alloying produces further intricacies in this structure, which our model explains. Compared to other halide perovskites, this class of materials shows unusually low absorption onset energies ranging between ca. 1.0 and 2.4 eV. Partial reduction of Au^{3+} to Au^+ affords an intervalence charge-transfer band, which redshifts the absorption onset of $Cs_8Au_4InCl_{23}$ from 2.4 to 1.5 eV. With connected Au−X octahedra and isolated M−X octahedra, this structure type combines zero- and three-dimensional metal-halide sublattices in a single material and stands out among halide perovskites for its ordering of homovalent metals, ordering of halide vacancies, and incorporation of purely trivalent metals at the octahedral sites.

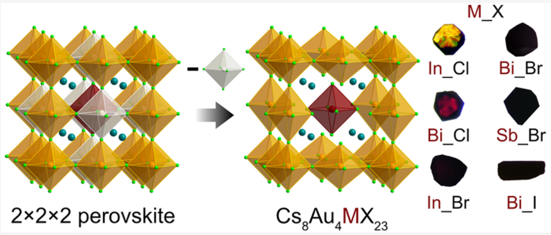

■ INTRODUCTION

The promising technological potential of halide perovskites as inexpensive solar-cell absorbers,[1] phosphors,[2,3] and light-emitting diodes[4] has reignited interest in this vast and well-known family of materials.[5] Research in this field is fueled by the synthetic tunability and structural definition of these crystalline solids, which are typically formed through solution-state self-assembly. Many possible combinations of A, B, and X within the ABX_3 (X = halide) perovskite framework give access to a large set of compositions. The B-site compositional flexibility offers perovskites with both main-group (B^{II} = Ge,[6] Sn,[7] Pb[8]) and transition-metal (B^{II} = Cd,[9] Hg,[9] Mn[10]) B-site occupants. Beyond the confines of the ABX_3 lattice, double perovskites ($2 \times AB^{II}X_3 \rightarrow A_2B_2X_6$; B = 1+, 3+, or 4+ metal or a vacancy) expand accessible B-site metals, affording the mixed-metal perovskites (e.g., $A_2BB'X_6$; B−B′ = Au^+−Au^{3+}, Ag^+−Au^{3+}, Tl^+−Tl^{3+}, Tl^+−Bi^{3+}, Ag^+−Bi^{3+}, Ag^+−In^{3+}, Ag^+−Sb^{3+}, Ag^+−Tl^{3+}, Na^+−Bi^{3+}, K^+−Bi^{3+}, and alkali-metal-rare-earth-metal combinations)[11−19] and perovskites with B-site vacancies (e.g., $A_2B\square X_6$; B = Sn^{4+}, Te^{4+}, Pd^{4+}, etc.).[20,21] Typically, ordered halide double perovskites form from heterovalent B-site metal combinations, such as the B^{1+}-B^{3+} metal pair, which has been studied since the 1920s,[11] and is now the subject of renewed interest.[22] Homovalent octahedral B-site metals (B^{2+}−B'^{2+}) typically yield solid solutions of single perovskites, where both metals are alloyed at the B sites instead of being ordered onto distinct crystallographic locations (e.g., $APb_xSn_{1-x}X_3$).[23,24]

The new mixed-metal perovskites presented here, $Cs_8Au^{III}_4M^{III}X_{23}$ (M = In^{3+}, Sb^{3+}, Bi^{3+}; X = Cl^-, Br^-, I^-), have a number of features that stand out even among the vast and diverse family of mixed-metal halide perovskites. To our knowledge, these constitute the first examples of a halide perovskite where the B site does not bear an average 2+ charge (see B-Site Charge in Halide Perovskites). Instead, charge compensation is provided through a stoichiometric halide vacancy whose ordering dictates the lattice symmetry. The six members of this new perovskite family have bandgaps across the visible spectrum, in contrast to the uniformly black Au^{3+} perovskites $Cs_2Ag^{I}Au^{III}X_6$ and $Cs_2Au^{I}Au^{III}X_6$ (X = Cl^-, Br^-, I^-).[11,25] The $Cs_8Au_4MX_{23}$ structure is composed of corner-sharing metal-halide octahedra tracing the edges of a cube, with an isolated metal-halide octahedron at the body center. It can be conceptually derived from the ABX_3 perovskite parent lattice in a manner similar to that of the $A_2B^{IV}\square X_6$ double

Received: February 9, 2021
Published: May 4, 2021

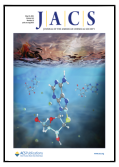

ACS Publications

https://doi.org/10.1021/jacs.1c01624

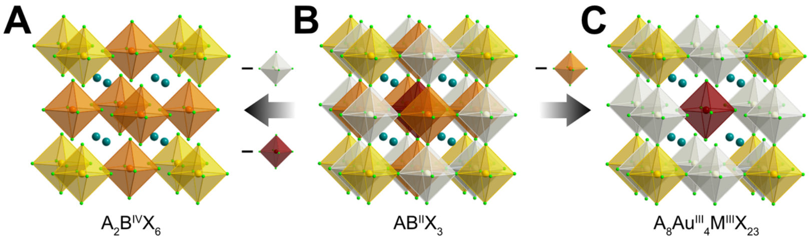

Figure 1. Conceptual derivation of perovskites with ordered vacancies by removing B-site metal atoms from (B) the 2 × 2 × 2 unit cell of the cubic $AB^{II}X_3$ perovskite. Metal coordination spheres are completed for clarity. (A) The double perovskite $A_2B^{IV}X_6$ is derived from part B by removing metal atoms from the body and edge centers. (C) The $A_8Au^{III}{}_4M^{III}X_{23}$ perovskite is derived from part B by removing metal atoms from the face centers. Metal-halide octahedra at the unit-cell corners, edge centers, face centers, and body center are represented in yellow, white, orange, and dark red, respectively. Teal and green spheres represent A- and X-site atoms, respectively.

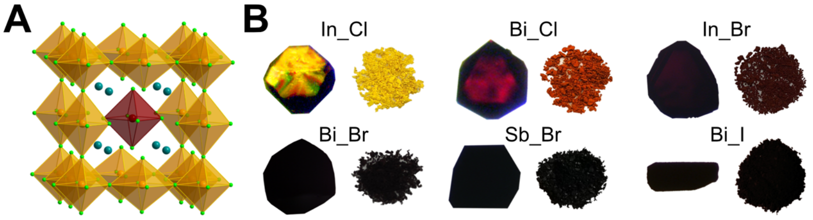

Figure 2. (A) Single crystal X-ray structure of $Cs_8Au_4InCl_{23}$ (**In_Cl**). Teal, gold, red, and green spheres represent Cs, Au, In, and Cl atoms, respectively. (B) Photographs of single crystals and powders of **In_Cl**, $Cs_8Au_4BiCl_{23}$ (**Bi_Cl**), $Cs_8Au_4InBr_{23}$ (**In_Br**), $Cs_8Au_4BiBr_{23}$ (**Bi_Br**), $Cs_8Au_4SbBr_{23}$ (**Sb_Br**), and $Cs_8Au_4BiI_{23}$ (**Bi_I**).

perovskites: whereas removal of metals at the body and edge centers of the 2 × 2 × 2 ABX_3 unit cell yields the $A_2B^{IV}\square X_6$ structure, removal of metals at the face centers affords the $A_8Au^{III}{}_4M^{III}\square_3X_{23}$ structure (Figure 1). Although there exist several examples of halide perovskites ordering elements with distinct oxidation states (e.g., A^{1+}−A^{2+} ordering in the layered $A^{I}{}_{n-1}A^{II}B_nX_{3n+1}$ Dion-Jacobson phases,[26] B^{1+}−B^{3+} cation ordering in $A_2B^{I}B^{III}X_6$ elpasolites,[27] and X^{1-}−X^{2-} ordering in the $ASbSI_2$ chalcogenide-halide perovskite[28]), ordered homovalent species within the halide perovskite family are comparatively rare. Akin to the $Cs_2Hg^{II}Pd^{II}Cl_6$ perovskite reported in 1991,[29] the $Cs_8Au^{III}{}_4M^{III}X_{23}$ perovskites presented here feature homovalent B-site ordering likely driven by local octahedral distortions rendering the two B sites symmetry inequivalent.

■ RESULTS AND DISCUSSION

1. B-Site Charge in Halide Perovskites. To our knowledge, any departure from divalent B-site metal selection in halide perovskites requires the resulting charge difference to be offset to preserve an average 2+ charge across B sites. For example, in elpasolites, with the general formula $A_2BB'X_6$, a B^{3+} metal is balanced by a B^{1+} metal, and a B^{4+} metal occurs along with a B-site vacancy. In related lattices, Bi^{3+} sits in 2/3 of the B sites, amending the typical 3D perovskite formula ($3 \times AB^{II}X_3 \rightarrow A_3B^{II}{}_3X_9 \rightarrow A_3B^{III}{}_2\square X_9$) to afford the layered derivatives $A_3Bi_2I_9$ (A = K, Rb).[30] Similarly, B^{2+} (Cd, Cu, Mn) and B^{3+} (Bi, Sb) are incorporated into a perovskite-derived lattice ($4 \times AB^{II}X_3 \rightarrow A_4B^{II}{}_4X_{12} \rightarrow A_4B^{II}B^{III}{}_2\square X_{12}$), yielding vacancies that layer the material.[31,32] The $A_2B_{2/3}X_4$ 2D perovskites provide yet another example of vacancies compensating for extra charge, with Bi^{3+} or Sb^{3+} placed on 2/3 of the B sites, leaving vacancies in the other 1/3 to provide charge balance.[33]

The perovskites described here constitute the first examples of a halide perovskite lattice where the B-site metal does not bear an average 2+ charge; instead, the 15/8 average charge of the B site is compensated by one halide vacancy per formula unit ($8 \times AB^{II}X_3 \rightarrow A_8B^{II}{}_8X_{24} \rightarrow Cs_8Au^{III}{}_4M^{III}\square_3X_{23}\square$), which we demonstrate can order under certain conditions.

2. Synthesis. The $Cs_8Au_4MX_{23}$ perovskites (M = In^{3+}, Sb^{3+}, Bi^{3+}; X = Cl^-, Br^-, I^-) were synthesized by dissolving the corresponding metal halides (CsX, $HAuCl_4 \cdot 3H_2O$, BiX_3) or metal oxides (In_2O_3, Sb_2O_3) in hot hydrohalic acid (HX) and cooling the solutions to precipitate the crystalline perovskites (see the Supporting Information for detailed procedures). Slowly cooling the precursor solution to room temperature over several hours produced truncated octahedral crystals with colors ranging from translucent amber for $Cs_8Au_4InCl_{23}$ (**In_Cl**) to translucent dark red for $Cs_8Au_4BiCl_{23}$ (**Bi_Cl**) and $Cs_8Au_4InBr_{23}$ (**In_Br**) and opaque black for $Cs_8Au_4BiBr_{23}$ (**Bi_Br**), $Cs_8Au_4SbBr_{23}$ (**Sb_Br**), and $Cs_8Au_4BiI_{23}$ (**Bi_I**) (Figure 2). Quickly cooling the hot precursor solution by dropping it directly into liquid nitrogen reduced the particle size,[34] producing yellow (**In_Cl**), orange (**Bi_Cl**), red (**In_Br**), brown (**Bi_Br**), and black (**Sb_Br** and **Bi_I**) polycrystalline powders. The elemental compositions of the bulk solids were assessed through inductively coupled plasma mass spectrometry (ICP−MS) (Tables S1 and S2). The crystals were kept in the mother liquor for storage and isolated by filtration for structural and optical characterization. Thermogravimetric analysis showed high thermal stability for **In_Cl**, with no mass loss up to a temperature of 350 °C (Figure S1), in contrast to organic−inorganic perovskites that lose volatile small molecules well below 100 °C.[35]

3. Structure of the Cubic Phase. The single-crystal X-ray diffraction (SCXRD) data of **In_Cl** were solved in the cubic space group $Pm\bar{3}m$ with a lattice parameter of 10.4943(3) Å at room temperature (Table S3). This structure features corner-sharing $[AuCl_6]^{3-}$ octahedra tracing the edges of a cube and an isolated $[InCl_6]^{3-}$ octahedron at its body center (Figure 2A). SCXRD gives analogous structures for **Bi_Cl**, **In_Br**, **Bi_Br**, **Sb_Br**, and **Bi_I** (Tables S5−S9). Experimental powder X-ray diffraction (PXRD) data from rapidly cooled powders and

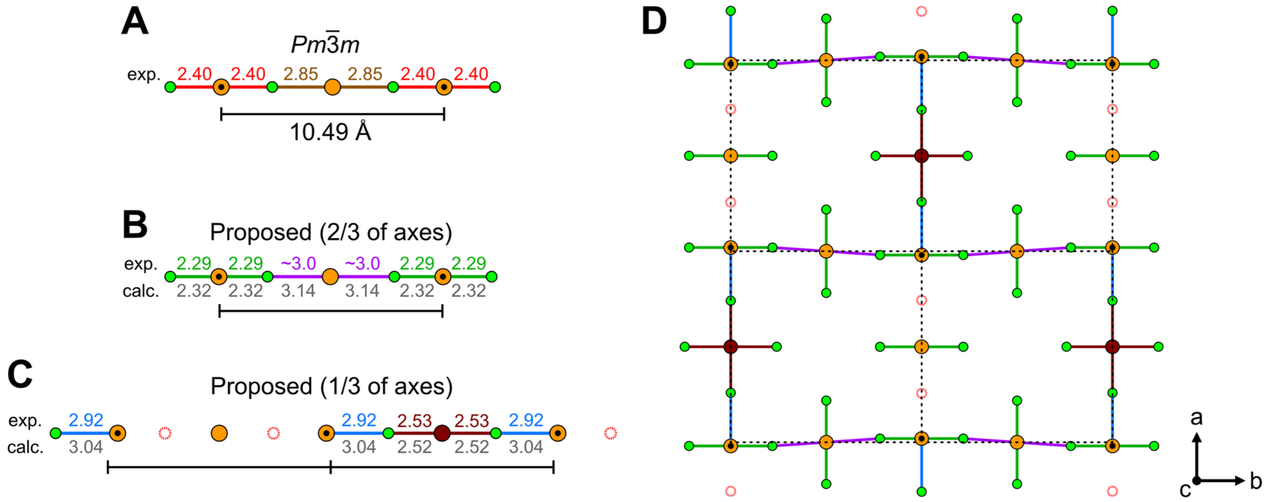

Figure 3. Illustrations of the local atomic structure of the gold-cage perovskites showing a single axis or plane and using **In_Cl** as an example. Gold, green, and dark red circles represent Au, Cl, and In atoms, respectively; dashed red circles represent Cl vacancies, and each black bar represents the experimentally determined unit-cell parameter. Au atoms at the unit-cell corners are denoted by a black dot in the center. Atoms perpendicular to the axis are omitted for clarity. (A) An illustration of the $Pm\bar{3}m$ structure solution. The bond lengths shown (in Å) derived from SCXRD are nonphysical values and each Cl shown has a site occupancy of 5/6 resulting from averaged disorder of a Cl vacancy. (B) An illustration of an axis with full Cl occupancy (on average constituting 2/3 of the axes). The bond lengths labeled "exp." shown (in Å) are derived from the PDF and EXAFS analysis, while those labeled "calc." are derived from computation. Overestimation of calculated lattice parameters and bond lengths is expected at this level of theory. (C) An illustration of an axis containing Cl vacancies (on average constituting 1/3 of the axes). This local structure would account for the crystallographic observations and elemental analysis. (D) An illustration of the (001) plane of the proposed local structure, with the observed unit-cell boundaries denoted by the dashed lines. See the Supporting Information for more details.

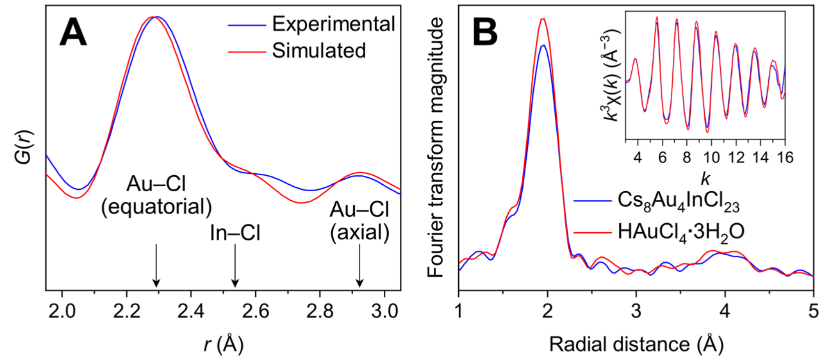

Figure 4. (A) Pair distribution function (PDF) analysis of **In_Cl**. The experimental PDF data (blue) show 2.29-Å and 2.92-Å Au−Cl bond distances (r), in agreement with data simulated from an SCXRD structure solution with nearest-neighbor Au−Cl bonds fixed at 2.29 Å (red). (B) Extended X-ray absorption fine structure (EXAFS) analysis from Au L_3-edge X-ray absorption spectroscopy (XAS) of **In_Cl**, plotted in k space (inset; extracted directly from XAS data after normalization) and Fourier-transformed to real space (main panel). The match between the data for **In_Cl** and $HAuCl_4 \cdot 3H_2O$ indicates a similar coordination environment for Au in both samples, with square-planar coordination of the nearest-neighbor Cl atoms at 2.29 Å. Note that bond lengths cannot be directly extracted from the radial distance but must be extracted from fitting the scattering paths, accounting for the phase shift.

PXRD patterns simulated from the SCXRD solutions are in good agreement (Figure S2). As anticipated from their Shannon radii,[36] replacement of In^{3+} ($R \approx 0.80$ Å) with Bi^{3+} ($R \approx 1.0$ Å) expands the lattice slightly (from $a = 10.4943(3)$ Å in **In_Cl** to $a = 10.5690(3)$ Å in **Bi_Cl**). A large increase in unit-cell dimensions occurs upon halide substitution: replacement of Cl^- ($R \approx 1.8$ Å) with Br^- ($R \approx 2.0$ Å) expands the lattice to 10.9116(2) Å and 10.9841(2) Å for **In_Br** and **Bi_Br**, respectively, while replacement of the halides with I^- ($R \approx 2.2$ Å) expands the lattice to 11.6645(5) Å for **Bi_I**.

The coordination sphere of the Au at the unit-cell edge centers (schematically depicted in white in Figure 1C) exhibits the tetragonal elongation expected for a d^8 Au^{3+} center, with the elongated axis oriented along the unit-cell edge, containing both bridging halides. However, the Au at the unit-cell corners (schematically depicted in yellow in Figure 1C) appears to be contained in a regular halide octahedron (Figure 2A). X-ray photoelectron spectroscopy (XPS) analysis indicates that **In_Cl** contains Au in its 3+ oxidation state (Figure S3), implying the existence of one Cl vacancy per formula unit for charge balance. The presence of a stoichiometric Cl vacancy was indeed corroborated by SCXRD: refining the chemical occupancy of all Cl atoms in the structure revealed 5/6 occupancy of the corner-Au-coordinating Cl atoms (bridging Cl atoms; Wyckoff position 6e) and full occupancy of the remaining terminal Cl atoms. These data suggest that although both unique Au sites in the structure experience the tetragonal elongation expected for a d^8 metal center, disorder of the fractional Cl occupancy is responsible for the unusual

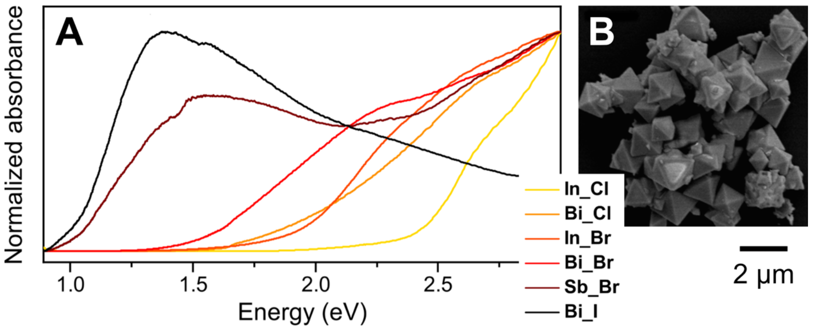

Figure 5. (A) UV−vis absorbance spectra of $Cs_8Au_4MX_{23}$ perovskite crystals pulverized into a mull with $BaSO_4$, converted from diffuse reflectance spectra using the Kubelka−Munk transformation, and normalized to the highest point at or below 3.0 eV. (B) SEM image of LN_2-precipitated crystals of **In_Cl**.

octahedral coordination environment observed for the corner Au in the $Pm\bar{3}m$ SCXRD solution.

The $Pm\bar{3}m$ solution for the SCXRD structure of **In_Cl** indicates that the Au atom at the unit-cell edge center (Wyckoff position 3d) possesses D_{4h} symmetry with four 2.32 Å equatorial (terminal) Au−Cl bonds and two 2.85 Å axial (bridging) Au−Cl bonds (Figure 3A, brown bonds). Though mirroring the [4 + 2] coordination symmetry of the Au^{3+} center in the $Cs_2Au^IAu^{III}Cl_6$ double perovskite, the $Pm\bar{3}m$ structure of **In_Cl** has shorter axial bonds than the 3.13 Å axial bonds of Au−Cl in $Cs_2Au^IAu^{III}Cl_6$.[27] In contrast, the Au atom at the unit-cell corner (Wyckoff position 1a) sits within a symmetry-constrained O_h coordination environment with six 2.40 Å Au−Cl bonds (Figure 3A, red bonds), where five Cl atoms are uniformly disordered over six sites. To further corroborate our structural model, we collected local structural information using pair distribution function (PDF) analysis. Indeed, PDF analysis of **In_Cl** and **Bi_Cl** points to 2.29 Å and ca. 2.92 Å Au−Cl bond distances in both materials with no indication of 2.40 Å bonds (Figures 4A and S4), implying that the corner Au also experiences a symmetry-lowering distortion but disorder is responsible for the averaging of axial and equatorial bond lengths in the $Pm\bar{3}m$ unit cell to yield an apparent Au−Cl bond distance of 2.40 Å. This disorder also results in the shortening of the axial (bridging) Au−Cl bonds of the edge-center Au from the expected 2.92 Å distance to the 2.85 Å distance observed in the $Pm\bar{3}m$ structure. The terminal Au−Cl bonds of this edge-center Au (2.32 Å) are not involved in the halide disorder, and the bond distances agree well with the PDF data (2.29 Å).

We collected X-ray absorption spectroscopy (XAS) data at the Au L_3-edge on $Cs_8Au_4MX_{23}$ to further probe the local structure of the Au centers. Similar to $HAuCl_4 \cdot 3H_2O$, which contains isolated square-planar $[AuCl_4]^-$ complexes with Au−Cl bond distances of 2.29 Å, the XAS data for **In_Cl** and **Bi_Cl** point to the 3+ oxidation state of Au and a square-planar Cl first coordination shell (Figures 4B and S5). Extended X-ray absorption fine structure (EXAFS) further supports this conclusion, indicating a Au−Cl bond distance of 2.289(7) Å and a coordination number of 3.9(5) for Au in **In_Cl**. Fitting the EXAFS data for **Bi_Cl** provides similar results, while fitting data for **In_Br**, **Bi_Br**, and **Sb_Br** gives an average Au−Br bond length of 2.436(4) Å and an average coordination number of 3.6(5) (Figure S6 and Table S10). The EXAFS data, however, are unable to provide reliable information about atoms beyond the first coordination shell of Au due to the overlap of multiple scattering paths (see the Supporting Information).

The local coordination geometry of Au determined by EXAFS and PDF, however, is not readily incorporated into the gold-cage crystal structure. The lattice parameter of the **In_Cl** cubic unit cell (10.49 Å) nearly matches the sum of the lengths of two short (2.29 Å) and two long (2.92 Å) Au−Cl bonds (Figure 3B), thus readily accommodating the two long axial bonds of the edge-center Au and two short bonds of the corner Au atoms. However, a unit-cell axis containing a long axial bond of a corner Au would contain three long and one short Au−Cl bonds, exceeding the limit imposed by the unit-cell dimensions (Figure S7A). Furthermore, this connectivity would result in halides that are bound only at axial positions to a Au center. Such interactions are unlikely to be stable: the vast majority of Au^{III}−halide complexes have square-planar geometry in the solid state,[37] whereas the few examples having [4 + 1] or [4 + 2] coordination have their axial halides stabilized by strong bonds to other metals or by hydrogen bonding. These constraints preclude an adequate structural description of the gold-cage structure with stoichiometric Au sites (Figure S7B,C). However, closer examination of SCXRD data reveals that the edge-center is a mixed atomic site, consisting of ca. 5/6 Au^{3+} and 1/6 M^{3+}, in agreement with ICP−MS elemental analysis of crystals that consistently provides a formula of ca. $Cs_8Au_{3.5}M_{1.5}X_{23}$ (Figure S8 and Table S2). This observation, coupled with the local coordination geometry of Au and the stoichiometric halide vacancy, allows for the complete structural description given below.

A given corner Au will have four short, coplanar equatorial bonds to bridging halides, an average of one long axial bond to a bridging halide, and one vacant axial coordination site. Every edge-center Au has its long axial bonds to bridging halides along the unit-cell axis on which it lies and four short bonds to terminal equatorial halides perpendicular to the unit-cell axis. For the two axes containing the short equatorial bonds of the corner Au atoms, the sum of the lengths of the two short equatorial bonds of the two corner Au atoms and the two long axial bonds of the edge-center Au in the middle is approximately equal to the unit-cell lattice parameter (Figure 3B).

But the halide bound axially to the corner Au will have only weak, unstable axial interactions (Figure S7). However, substitution of the edge-center Au on this unit-cell axis with an octahedrally coordinated M^{3+} ion provides a strong bond to this halide (Figure 3C). This substitution further enforces a

https://doi.org/10.1021/jacs.1c01624
J. Am. Chem. Soc. 2021, 143, 7440−7448

halide vacancy in the adjacent unit cells along the same axis, causing each of the corner $[AuX_5]^{2-}$ units to move closer to the adjacent halide vacancy to accommodate the $[MX_6]^{3-}$ octahedron (Figures 3C and S9). This structural description results in an average of 1/6 occupancy of the edge-centers with M^{3+} and one halide vacancy per corner Au, giving a formula of $Cs_8Au_{3.5}M_{1.5}X_{23}$ (Figure S8), which matches the formula derived from ICP−MS elemental analysis and SCXRD (see the SI and Figures S9 and S10 for a more detailed discussion).

4. Symmetry Lowering through Ordered Halide Vacancies. The spatial distribution of halide vacancies was found to be influenced by sample preparation: fast precipitation of the product by dropping the hot precursor solution directly into liquid nitrogen[34] yielded powders showing PXRD data in good agreement with PXRD data simulated from the $Pm\bar{3}m$ SCXRD solution. Scanning electron microscopy (SEM) imaging revealed the rapidly precipitated powders are composed of octahedral crystallites with sizes on the order of 1 μm (Figures 5B and S11). Samples obtained by slowly cooling the same precursor solution and pulverizing the resulting crystals showed more complex PXRD patterns with pronounced peak splitting (Figures S12 and S13 and Table S12). This symmetry reduction apparent in the PXRD data of slow-cooled samples inspired a reexamination of the SCXRD data in pursuit of a lower-symmetry solution.

With symmetry breaking in mind, a second SCXRD solution for **In_Cl** was obtained in the tetragonal space group $P4/mmm$ (Table S3). This is the highest-symmetry space group allowing for the tetragonal distortion of the Au center at the unit-cell corner, offering the PDF- and XAS-supported axial and equatorial Au−X bond lengths. The $P4/mmm$ SCXRD structure solution for **In_Cl** was solved with unit-cell parameters $a = b = 10.4449(3)$ Å and $c = 10.5714(3)$ Å obtained from Rietveld analysis carried out on high-resolution synchrotron PXRD (HR-PXRD) data collected on pulverized slow-cooled crystals of **In_Cl**. This SCXRD solution features a 2.35 Å corner Au−Cl bond along the c-axis, more closely matching the 2.29 Å bond length indicated by PDF and EXAFS than the 2.40 Å Au−Cl bond length of the $Pm\bar{3}m$ solution (see the SI for more details). However, the tetragonal solution still retains nonphysical 2.41 Å Au−Cl bond lengths along the a- and b-axes. Freely refining the occupancies of the two crystallographically unique Cl atoms bonded to the corner Au in this solution results in ca. 90% occupancy of the Cl parallel to the c-axis and ca. 80% occupancy of the Cl in the (001) crystallographic plane, indicating a preference of the Cl vacancy for the (001) plane. Analysis of the thermal ellipsoids of the Au and Cl atoms and residual electron density maps of the $P4/mmm$ structure support a similar structural model as that proposed for the $Pm\bar{3}m$ structure (see Structure of the Cubic Phase) but with a preference for the Cl vacancies to occupy the (001) plane. Indeed, the substitution of the edge-center Au with In is inversely correlated with the occupancy of the bridging Cl along the same axis in the SCXRD solution, as expected for this structural model (Figure 3C). The HR-PXRD analysis and SCXRD solutions for **Bi_Cl**, **In_Br**, **Bi_Br**, **Sb_Br**, and **Bi_I** in $P4/mmm$ reveal similar tetragonal distortions and halide vacancy and M^{3+} ordering. Additionally, the corner Au−Br bond length along the c-axis is 2.45 Å, 2.44 Å, and 2.47 Å in **In_Br**, **Bi_Br**, and **Sb_Br**, respectively, in good agreement with the 2.44 Å bond length extracted from EXAFS (Table S10). Such analysis supports the $P4/mmm$ space-group assignment and halide-vacancy and M^{3+} ordering within this family of perovskites.

While not uncommon in oxide perovskites, with examples such as $PrBaMn_2O_5$[38] and $CaMnO_{2.5}$,[39] crystallographically ordered anion vacancies are rare in halide perovskites. Halide vacancies have been implicated in the high halide conductivity of halide perovskites[40,41] and have been shown to occur spontaneously[34] or as a charge-compensating mechanism for heterovalent impurity alloying.[42] In the case of the $Cs_8Au_4MX_{23}$ family presented here, three chemically inequivalent halide sites exist in the cubic $Pm\bar{3}m$ unit cell: those lying along the unit-cell edge (bridging, Wyckoff position 6e), at the unit-cell face (terminal, Wyckoff position 12h), and within the unit-cell interior (terminal, Wyckoff position 6f). We used density functional theory (DFT) to explore the effect of the vacancy position on the computed ground-state energy using the cubic $Pm\bar{3}m$ unit cell as a starting point for relaxation. As compared with the observed bridging Cl vacancy at the unit-cell edge, structural isomers of **In_Cl** with the Cl vacancy placed at a terminal position at the unit-cell face or within the interior had calculated total energies that were higher by 7 and 33 meV/atom in the relaxed tetragonal unit cell, respectively (Figure S14 and Table S13). This trend is retained in the 1 × 2 × 2 supercells (see Electronic Structure), where placing the vacancy at the unit-cell face or within the interior yielded energies that were higher by 7 and 42 meV/atom upon relaxation, respectively. This analysis supports the observed absence of the Cl atom along the unit-cell edge as the most favorable placement of the charge-compensating vacancy. Furthermore, because the $Cs_8Au_4MX_{23}$ lattice dimensions are primarily set by contacts between Au atoms and the bridging halides, halide removal from the (001) plane of the hypothetical $Cs_8Au_4MX_{24}^{-}$ is accompanied by contraction of the a- and b-axes, as is observed in the SCXRD and PXRD data.

Given the importance of vacancy-assisted halide migration in the ionic conductivity of halide perovskites[40,43] and the unusually high concentration of such defects in $Cs_8Au_4MX_{23}$ (ca. 4% in $Cs_8Au_4MX_{23}$ and 0.4% in $(CH_3NH_3)PbI_3$[44]), we sought to determine if the halide vacancies in $Cs_8Au_4MX_{23}$ were mobile. Electrochemical impedance spectroscopy (EIS) measurements on both single crystals and pressed powders of **In_Cl** using carbon electrodes indicate low ionic conductivity (Figure S15 and Table S14).[45] This low ionic conductivity may be rationalized by the high barrier for M^{III}−X bond breaking or metal reorganization that would be required for halide mobility in the proposed structural model (see Structure of the Cubic Phase). Additionally, a low halide mobility is consistent with the persistence of $Pm\bar{3}m$ symmetry in rapidly precipitated powders: no observable cubic-to-tetragonal peak splitting in the PXRD data during months of storage indicates that halides are frozen in place at room temperature.

5. Optical Properties. We next turned our attention to the optical properties of the $Cs_8Au_4MX_{23}$ perovskites. Crystals of $Cs_8Au_4MX_{23}$ were diluted and pulverized into a mull with $BaSO_4$ for ultraviolet−visible−near-infrared diffuse reflectance (UV−vis) spectroscopy measurements. The data were transformed to pseudoabsorbance using the Kubelka−Munk theorem.[46] The resulting spectra were normalized to high-energy absorption features and the absorption onsets were roughly estimated as the energy when the absorbance reached 0.1 AU. Solids **In_Cl** and **Bi_Cl** have absorption onsets at 2.4 and 1.9 eV, respectively, **In_Br**, **Bi_Br**, and **Sb_Br** show absorption onsets at 1.9, 1.6, and 1.1 eV, respectively, and **Bi_I** shows an absorption onset at 1.0 eV (Figures 5A and S16). In accordance with the general trend observed in halide perovskites,[47] UV−vis spectra reveal a redshift of the absorption onset with decreasing electronegativity of the halide (Figure 5A, **Bi_X** (X = Cl, Br, and I)). Replacement of In^{3+} with Bi^{3+} also causes a redshift in $Cs_8Au_4MX_{23}$. A similar redshift is observed in the double perovskite $Cs_2AgInCl_6$, where substitution of Bi^{3+} for In^{3+} to form the isostructural $Cs_2AgBiCl_6$ results in a 0.5 eV bandgap reduction.[14,15] This is ascribed to the participation of Bi s orbitals at the top of the valence band that increase the energy of the valence-band maximum relative to the In-containing analog.[15] Precipitation of $Cs_8Au_4MX_{23}$ perovskites by rapid cooling in liquid nitrogen increases the magnitude of low-energy absorption compared to that of the slow-cooled crystals (Figure S17), which may be due to the halide-vacancy disorder afforded by rapid precipitation (see Symmetry Lowering through Ordered Halide Vacancies).

Due to the effect of crystallization dynamics on the steepness of the absorption onset, we do not assign the direct/indirect nature of the bandgap using Tauc plots obtained through diffuse reflectance measurements. But the energy at which the absorption becomes sharp is minimally dependent on the crystallization kinetics and is red-shifted with respect to common halide single and double perovskites, for example, $CsPbBr_3$ (E_g = 2.3 eV),[48] $CsPbCl_3$ (E_g = 2.9 eV),[48] and $Cs_2AgBiBr_6$ (E_g = 2.0 eV).[13] To our knowledge, such low-energy absorption in Cl and Br perovskites has only been observed in the gold-based double perovskites $Cs_2Ag^IAu^{III}X_6$ and $Cs_2Au^IAu^{III}X_6$,[25] and, more recently, in the $Cs_2Ag^ITl^{III}X_6$ double perovskites.[34]

6. Alloying the Metal Sites. The yellow solid shown for **In_Cl** in Figure 2B was obtained by cooling solutions of CsCl, $HAuCl_4$, and $InCl_3$ in a 4:1:1 molar ratio, respectively. Upon Au^{3+} enrichment of the precursor solution, however, a darker solid precipitated. By adjusting the Au^{3+}:In^{3+} molar ratio in the precursor solution from 1:1 to 6:1, we could continuously tune the color of the resulting crystals from translucent yellow to opaque black, with a corresponding increase in a new low-energy UV−vis absorption band (Figure 6). Solution Au^{3+}:In^{3+} ratios below 1 and above 6 yielded $Cs_2InCl_5{\cdot}H_2O$ and $CsAuCl_4$ side products, respectively (Figure S18).

The observed yellow-to-black color change with increasing Au^{3+} in solution is consistent with the incorporation of a Au^+ impurity in the **In_Cl** lattice. Two observations support this conclusion: (1) the darkening is prevented by the addition of a few drops of nitric acid to the crystallization solution, which can oxidize Au^+ ions to Au^{3+} ions (Figure 6B, yellow trace), and (2) the darkening increases upon extending the time the solution is kept at elevated temperature. The intensity of the low-energy absorption feature also increases significantly (Figure 6B, black trace) when the solution cooling time is extended from hours to days, suggesting greater conversion of Au^{3+} to Au^+. We note that this low-energy absorption feature coincides with the intervalence charge-transfer band seen in the absorption spectrum of the double perovskite $Cs_2Au^IAu^{III}Cl_6$ (Figures S19 and S20),[25,49] supporting the hypothesis of mixed valence in Au-rich **In_Cl**. No Au^+ was detected in XAS or XPS analysis, indicating that a small concentration of Au^I−Cl−Au^{III} units in the lattice is likely sufficient to dominate the absorption onset of **In_Cl**.

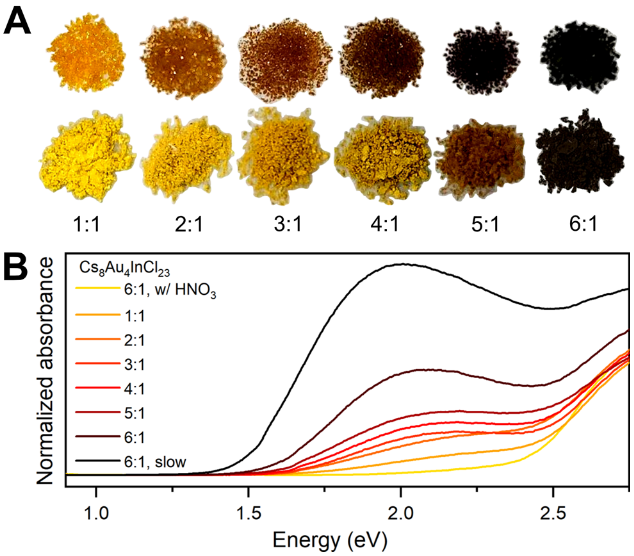

Figure 6. (A) Photographs of crystals (top panel) and powders (bottom panel) of **In_Cl** with progressively more Au^+ alloyed into the structure from left to right. (B) UV−vis absorbance spectra converted from diffuse reflectance spectra using the Kubelka−Munk transformation showing an increase in low-energy absorption of **In_Cl** with Au^+ alloying. The values in the legend refer to the ratio of Au^{3+} to In^{3+} in the crystallization solution. The trace labeled "slow" refers to a sample that was cooled more slowly than the others, thus resulting in a higher concentration of Au^+ and therefore a stronger low-energy absorption feature. The spectra are normalized to a peak at 3.8 eV.

In addition to Au^+ alloying into **In_Cl**, the homovalent Au^{3+} and body-center M^{3+} metals can alloy onto each other's crystallographic sites. As discussed in Structure of the Cubic Phase and Symmetry Lowering through Ordered Halide Vacancies, M^{3+} ions occupy 1/6 of the edge-center sites, independent of the ratio of Au^{3+} to M^{3+} in the crystallization solution. Further, under Au-rich synthetic conditions, SCXRD indicates that the body-center site of **In_Cl** contains a mixture of 97% In and 3% Au. Indeed, the PXRD reflections shift to slightly lower 2θ values, consistent with a small expansion of the lattice accommodating the comparatively larger Au^{3+} cation at the body center (Figure S20). We note that the X-ray scattering factors for Au and Bi are too similar to reliably distinguish the two elements, precluding this analysis in **Bi_Cl**, **Bi_Br**, and **Bi_I**. Indeed, structure solutions for these analogs show no significant deviations in the occupancies of the metal sites from unity when freely refined.

7. Electronic Structure. We performed DFT calculations of **In_Cl** and **Bi_Cl** using 1 × 2 × 2 supercells; this allowed us to capture the experimentally observed halide vacancy disorder and the alloying that occurs between Au^{3+} and M^{3+} at the edge-center sites to form $Cs_8Au_{3.5}M_{1.5}X_{23}$, as proposed by the structural model (Figures 3, S8, and S26). Using the cubic $Pm\bar{3}m$ unit cell as a starting point, structural relaxations were carried out with the Perdew−Burke−Ernzerhof (PBE) exchange-correlation functional as implemented with VASP (see the SI for details).[50,51] In agreement with the PDF analysis and Rietveld characterization, our DFT−PBE calculations of **In_Cl** predict axial elongation of Au−Cl bonds and a metrically tetragonal structure when one Cl atom bound to the corner Au is removed per unit cell (Figure S27). Additionally, the $[AuCl_5]^{2-}$ units move closer to the vacant

Cl sites upon relaxation with DFT, consistent with the proposed structural model intuited from experimental observations (Figures 3D and S27; see Structure of the Cubic Phase). Analogous relaxations of the 1 × 2 × 2 supercell of **Bi_Cl** yield a similar structure, with a slight elongation of the lattice constants resulting in a ca. 2.5% increase of the supercell volume with respect to that of **In_Cl**.

Although we underestimate the experimental bandgap values, as expected using DFT−PBE, our calculations show that replacing In^{3+} with Bi^{3+} reduces the bandgap by 0.57 eV, similar to the 0.5 eV reduction observed experimentally. Both the valence and conduction bands contain Cl p-orbital states (Figure S28 and Table S15) and the low-lying conduction bands of **In_Cl** also have significant Au d-orbital character, whereas In has a negligible contribution to the band extrema (Figure 7A). In contrast, the band structure of **Bi_Cl** indicates that Bi s-orbital states are hybridized with the valence bands and raise the energy of the valence-band maximum to reduce the bandgap relative to that of **In_Cl** (Figure 7B). Comparing this edge-alloyed structure to an analogous 1 × 2 × 2 supercell of **Bi_Cl** where Bi is only present at the body center and is not alloyed at the edge-center sites, we find the Bi s states are no longer present at the valence-band maximum and the bandgap is reduced by 60 meV (Figure S28 and Table S15). These results indicate that increasing the Au content decreases the bandgap; indeed, a similar calculation using a 1 × 2 × 2 supercell of the hypothetical Cs$_8$Au$_5$Cl$_{23}$, constructed analogously to the 1 × 2 × 2 supercells used for **In_Cl** and **Bi_Cl**, yields a metallic band structure (Table S15). We can further understand the bandgap trends by calculating the gaps of hypothetical compounds with M^{3+} cations replacing all Au^{3+} cations: we find bandgap values of 2.17 eV for Cs$_8$In$_5$Cl$_{23}$ and 1.36 eV for Cs$_8$Bi$_5$Cl$_{23}$ for relaxed single unit cells (Table S16; see the SI for details), supporting the lower bandgap of **Bi_Cl** compared to that of **In_Cl**.

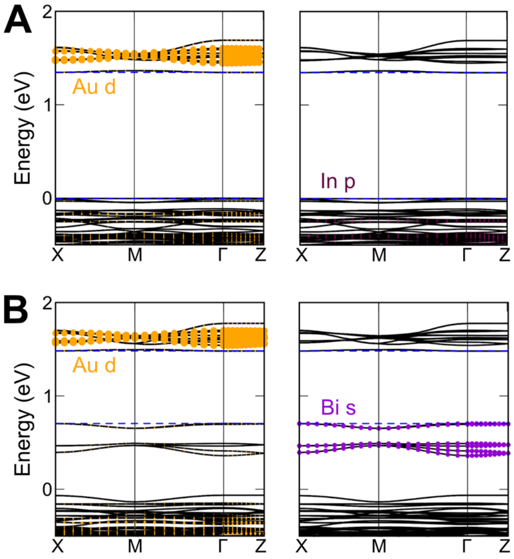

Figure 7. Calculated DFT−PBE band structures of the relaxed 1 × 2 × 2 supercells with the formula Cs$_8$Au$_{3.5}$M$_{1.5}$Cl$_{23}$ of (A) **In_Cl** and (B) **Bi_Cl** showing contributions from Au (left) and In or Bi atoms (right). The In p-orbital contribution to the valence bands is <1% in part A. All bands are shifted to align the Cs 5s bands and the zero energy is set to the valence-band maximum of **In_Cl**. The valence- and conduction-band extrema are denoted by the blue dashed lines.

CONCLUSIONS

The Cs$_8$Au$^{III}_4$M^{III}X$_{23}$ (M = In^{3+}, Sb^{3+}, Bi^{3+}; X = Cl$^-$, Br$^-$, I$^-$) gold-cage compounds exhibit a novel structure in the halide perovskite family. By maintaining stoichiometric halide vacancies, this material also provides the only counter example to the postulate that all halide perovskites maintain an average B-site charge of 2+ (averaging over both occupied and unoccupied B sites). The placement of the halide vacancies can be controlled through the crystallization kinetics, with fast and slow cooling affording fully disordered and partially ordered halide vacancies, respectively, around the corner Au. We propose a structural model that explains the X-ray diffraction, XAS, and PDF data and elemental analyses and is supported by DFT calculations. This structure offers several other deviations from the typical perovskite lattice, including containing exclusively trivalent B-site metals, ordering homovalent chemical species onto distinct crystallographic sites, and ordering halide vacancies along crystallographic planes.

These semiconductors have absorption onsets spanning the visible and near-infrared, affording colored solids from translucent yellow (Cs$_8$Au$_4$InCl$_{23}$) to opaque black (Cs$_8$Au$_4$BiI$_{23}$). Partial alloying at the metal sites plays an important role in the optical absorption of these materials. Alloying Au$^+$ affords a yellow-to-black color change in Cs$_8$Au$_4$InCl$_{23}$ and an intervalence charge-transfer absorption band centered at 2.0 eV. The optical absorption onsets of the new Cs$_8$Au$_4$MX$_{23}$ perovskites span the ideal bandgap ranges for absorbers in single-junction solar cells (1.4 eV) and for absorbers in tandem solar cells (e.g., ca. 1 eV for the bottom absorber in an all-perovskite device and 1.8 eV for the top absorber with Si).[52] As such, the dynamics of photogenerated carriers in these materials warrant further study. With unprecedented structure and absorption that is tunable across the visible spectrum, the Cs$_8$Au$^{III}_4$M^{III}X$_{23}$ family of perovskites presented in this work expands ordered mixed-metal perovskite compositions beyond the prototypical elpasolite B^{1+}−B^{3+} pair[53] and demonstrates the promise of studying new perovskite architectures.

ASSOCIATED CONTENT

Supporting Information

The Supporting Information is available free of charge at https://pubs.acs.org/doi/10.1021/jacs.1c01624.

Experimental details, crystallographic data, and spectra (PDF)

Accession Codes

CCDC 2023718−2023731 contain the supplementary crystallographic data for this paper. These data can be obtained free of charge via www.ccdc.cam.ac.uk/data_request/cif, or by emailing data_request@ccdc.cam.ac.uk, or by contacting The Cambridge Crystallographic Data Centre, 12 Union Road, Cambridge CB2 1EZ, UK; fax: +44 1223 336033.

AUTHOR INFORMATION

Corresponding Author

Hemamala I. Karunadasa − *Department of Chemistry, Stanford University, Stanford, California 94305, United States; Stanford Institute for Materials and Energy Sciences, SLAC National Accelerator Laboratory, Menlo Park, California 94025, United States;* orcid.org/0000-0003-4949-8068; Email: hemamala@stanford.edu

Authors

Kurt P. Lindquist − *Department of Chemistry, Stanford University, Stanford, California 94305, United States*

Michael A. Boles − *Department of Chemistry, Stanford University, Stanford, California 94305, United States*

Stephanie A. Mack − *Department of Physics, University of California Berkeley, Berkeley, California 94720, United States; Materials Sciences Division, Lawrence Berkeley National Laboratory, Berkeley, California 94720, United States*

Jeffrey B. Neaton − *Department of Physics, University of California Berkeley, Berkeley, California 94720, United States; Materials Sciences Division, Lawrence Berkeley National Laboratory, Berkeley, California 94720, United States; Kavli Energy NanoScience Institute at Berkeley, Berkeley, California 94720, United States*

Complete contact information is available at:
https://pubs.acs.org/10.1021/jacs.1c01624

Author Contributions

[$] K.P.L. and M.A.B. contributed equally to this work.

Notes

The authors declare no competing financial interest.

■ ACKNOWLEDGMENTS

This work was supported by the Department of Energy (DOE), Office of Basic Energy Sciences, Division of Materials Sciences and Engineering, under contract DE-AC02-76SF00515. K.P.L. thanks the Center for Molecular Analysis and Design at Stanford University for a graduate fellowship and the Stanford Department of Chemistry for the William S. Johnson award. M.A.B. gratefully acknowledges support from the Camille and Henry Dreyfus Postdoctoral Program in Environmental Chemistry. We thank Dr. K. Beyer at Argonne National Laboratory (ANL) for PDF data collection, Dr. D. Umeyama for assistance with PDF data processing, and Dr. S. J. Teat at Lawrence Berkeley National Laboratory (LBNL) for assistance with crystallography. SCXRD studies were performed at beamline 12.2.1 at the Advanced Light Source (ALS) at LBNL. XPS, SEM, and additional SCXRD studies were performed at the Stanford Nanocharacterization Laboratory (SNL) and DSC studies were performed at the Soft & Hybrid Materials Facility (SMF), both part of the Stanford Nano Shared Facilities (SNSF), supported by the National Science Foundation under award ECCS-1542152. XAS studies used beamline 2-2 at SSRL at the SLAC National Accelerator Laboratory. PDF studies used beamline 11-ID-B and HR-PXRD studies used beamline 11-BM at the Advanced Photon Source, a U.S. DOE Office of Science User Facility operated for the DOE Office of Science by ANL under Contract No. DE-AC02-06CH11357. Work by J.B.N. and S.A.M. was funded by the Department of Energy (DOE), Office of Basic Energy Sciences, Division of Materials Sciences and Engineering (Theory FWP), under contract DE-AC02-05CH11231. Additional computational resources were provided by NERSC. Work at the Molecular Foundry and the ALS was supported by the DOE, Office of Basic Energy Sciences (DE-AC02-05CH11231).

■ REFERENCES

(1) Green, M. A.; Ho-Baillie, A.; Snaith, H. J. The Emergence of Perovskite Solar Cells. *Nat. Photonics* **2014**, *8*, 506−514.

(2) Kovalenko, M. V.; Protesescu, L.; Bodnarchuk, M. I. Properties and potential optoelectronic applications of lead halide perovskite nanocrystals. *Science* **2017**, *358* (6364), 745−750.

(3) Smith, M. D.; Connor, B. A.; Karunadasa, H. I. Tuning the Luminescence of Layered Halide Perovskites. *Chem. Rev.* **2019**, *119* (5), 3104−3139.

(4) Kim, Y. H.; Cho, H.; Lee, T. W. Metal halide perovskite light emitters. *Proc. Natl. Acad. Sci. U. S. A.* **2016**, *113* (42), 11694−11702.

(5) Saparov, B.; Mitzi, D. B. Organic−Inorganic Perovskites: Structural Versatility for Functional Materials Design. *Chem. Rev.* **2016**, *116* (7), 4558−4596.

(6) Christensen, A. N.; Rasmussen, S. E. A Ferroelectric Chloride of Perowskite Type: Crystal Structures of $CsGeCl_3$. *Acta Chem. Scand.* **1965**, *19*, 421−428.

(7) Yamada, K.; Funabiki, S.; Horimoto, H.; Matsui, T.; Okuda, T.; Ichiba, S. Structural Phase Transitions of the Polymorphs of $CsSnI_3$ by Means of Rietveld Analysis of the X-Ray Diffraction. *Chem. Lett.* **1991**, *20* (5), 801−804.

(8) Møller, C. K. A Phase Transition in Cæsium Plumbochloride. *Nature* **1957**, *180* (4593), 981−982.

(9) Natta, G.; Passerini, L. Isomorfismo, Polimorfismo e Morfotropia.—I. Composti del Tipo ABX_3. *Gazz. Chim. Ital.* **1928**, *58*, 472−484.

(10) van Arkel, A. E. Kristalstructuur van Magnesiumfluoride en Andere Verbindingen van Hetzelfde Kristaltype. *Physica* **1925**, *5*, 162−171.

(11) Wells, H. L. Some Complex Chlorides containing Gold. II. Cesium Triple Salts. *Am. J. Sci.* **1922**, *3* (17), 315−326.

(12) Retuerto, M.; Emge, T.; Hadermann, J.; Stephens, P. W.; Li, M. R.; Yin, Z. P.; Croft, M.; Ignatov, A.; Zhang, S. J.; Yuan, Z.; Jin, C.; Simonson, J. W.; Aronson, M. C.; Pan, A.; Basov, D. N.; Kotliar, G.; Greenblatt, M. Synthesis and Properties of Charge-Ordered Thallium Halide Perovskites, $CsTl^{+}{}_{0.5}Tl^{3+}{}_{0.5}X_3$ (X = F or Cl): Theoretical Precursors for Superconductivity? *Chem. Mater.* **2013**, *25* (20), 4071−4079.

(13) Slavney, A. H.; Hu, T.; Lindenberg, A. M.; Karunadasa, H. I. A Bismuth-Halide Double Perovskite with Long Carrier Recombination Lifetime for Photovoltaic Applications. *J. Am. Chem. Soc.* **2016**, *138* (7), 2138−41.

(14) McClure, E. T.; Ball, M. R.; Windl, W.; Woodward, P. M. Cs_2AgBiX_6 (X = Br, Cl): New Visible Light Absorbing, Lead-Free Halide Perovskite Semiconductors. *Chem. Mater.* **2016**, *28* (5), 1348−1354.

(15) Volonakis, G.; Haghighirad, A. A.; Milot, R. L.; Sio, W. H.; Filip, M. R.; Wenger, B.; Johnston, M. B.; Herz, L. M.; Snaith, H. J.; Giustino, F. $Cs_2InAgCl_6$: A New Lead-Free Halide Double Perovskite with Direct Band Gap. *J. Phys. Chem. Lett.* **2017**, *8* (4), 772−778.

(16) Tran, T. T.; Panella, J. R.; Chamorro, J. R.; Morey, J. R.; McQueen, T. M. Designing indirect−direct bandgap transitions in double perovskites. *Mater. Horiz.* **2017**, *4* (4), 688−693.

(17) Morss, L. R.; Siegal, M.; Stenger, L.; Edelstein, N. Preparation of Cubic Chloro Complex Compounds of Trivalent Metals: Cs_2NaMCl_6. *Inorg. Chem.* **1970**, *9* (7), 1771−1775.

(18) Wei, F.; Deng, Z.; Sun, S.; Xie, F.; Kieslich, G.; Evans, D. M.; Carpenter, M. A.; Bristowe, P. D.; Cheetham, A. K. The synthesis, structure and electronic properties of a lead-free hybrid inorganic−organic double perovskite $(MA)_2KBiCl_6$ (MA = methylammonium). *Mater. Horiz.* **2016**, *3* (4), 328−332.

(19) Deng, Z. Y.; Wei, F. X.; Sun, S. J.; Kieslich, G.; Cheetham, A. K.; Bristowe, P. D. Exploring the properties of lead-free hybrid double perovskites using a combined computational-experimental approach. *J. Mater. Chem. A* **2016**, *4* (31), 12025−12029.

(20) Dickinson, R. G. The Crystal Structures of Potassium and Ammonium Chlorostannates. *J. Am. Chem. Soc.* **1922**, *44* (2), 276−288.

(21) Engel, G. Die Kristallstrukturen einiger Verbindungen vom K_2PtCl_6-Typ. *Naturwissenschaften* **1933**, *21* (39), 704−704.

(22) Giustino, F.; Snaith, H. J. Toward Lead-Free Perovskite Solar Cells. *ACS Energy Lett.* **2016**, *1* (6), 1233−1240.

(23) Donaldson, J. D.; Laughlin, D.; Ross, S. D.; Silver, J. Phases obtained from the Frozen Molten Systems Caesium−Tin−Halide and Caesium−Lead−Halide. *J. Chem. Soc., Dalton Trans.* **1973**, No. 19, 1985−1988.

(24) Barrett, J.; Donaldson, J. D.; Silver, J.; Siew, N. P. Y. Mössbauer and Electronic-reflectance Spectroscopic Studies and Resistivity Measurements on the Systems $CsPb_{1-x}Sn_xBr_3$, $CsPb_{1-x}Sn_xBr_2Cl$, $M_xCs_{1-x}SnBr_3$, and $M_xCs_{1-x}SnBr_2Cl$ (M = Na, K, Rb, and NH_4). *J. Chem. Soc., Dalton Trans.* **1977**, No. 9, 906−908.

(25) Kojima, N.; Kitagawa, H. Optical Investigation of the Intervalence Charge-transfer Interactions in the Three-dimensional Gold Mixed-valence Compounds $Cs_2Au_2X_6$ (X = Cl, Br or I). *J. Chem. Soc., Dalton Trans.* **1994**, No. 3, 327−331.

(26) Mao, L.; Ke, W.; Pedesseau, L.; Wu, Y.; Katan, C.; Even, J.; Wasielewski, M. R.; Stoumpos, C. C.; Kanatzidis, M. G. Hybrid Dion−Jacobson 2D Lead Iodide Perovskites. *J. Am. Chem. Soc.* **2018**, *140* (10), 3775−3783.

(27) Elliott, N.; Pauling, L. The Crystal Structure of Cesium Aurous Auric Chloride, $Cs_2AuAuCl_6$, and Cesium Argentous Auric Chloride, $Cs_2AgAuCl_6$. *J. Am. Chem. Soc.* **1938**, *60* (8), 1846−1851.

(28) Nie, R.; Mehta, A.; Park, B. W.; Kwon, H. W.; Im, J.; Seok, S. I. Mixed Sulfur and Iodide-Based Lead-Free Perovskite Solar Cells. *J. Am. Chem. Soc.* **2018**, *140* (3), 872−875.

(29) Schröder, L.; Keller, H.-L. Darstellung und Kristallstruktur von $Cs_2HgPdCl_6$, eine Verzerrungsvariante der Chloroperowskite. *Z. Anorg. Allg. Chem.* **1991**, *603* (1), 69−76.

(30) Lehner, A. J.; Fabini, D. H.; Evans, H. A.; Hébert, C.-A.; Smock, S. R.; Hu, J.; Wang, H.; Zwanziger, J. W.; Chabinyc, M. L.; Seshadri, R. Crystal and Electronic Structures of Complex Bismuth Iodides $A_3Bi_2I_9$ (A = K, Rb, Cs) Related to Perovskite: Aiding the Rational Design of Photovoltaics. *Chem. Mater.* **2015**, *27* (20), 7137−7148.

(31) Vargas, B.; Ramos, E.; Perez-Gutierrez, E.; Alonso, J. C.; Solis-Ibarra, D. A Direct Bandgap Copper−Antimony Halide Perovskite. *J. Am. Chem. Soc.* **2017**, *139* (27), 9116−9119.

(32) Holzapfel, N. P.; Majher, J. D.; Strom, T. A.; Moore, C. E.; Woodward, P. M. $Cs_4Cd_{1-x}Mn_xBi_2Cl_{12}$—A Vacancy-Ordered Halide Perovskite Phosphor with High-Efficiency Orange-Red Emission. *Chem. Mater.* **2020**, *32* (8), 3510−3516.

(33) Mitzi, D. B. Organic−Inorganic Perovskites Containing Trivalent Metal Halide Layers: The Templating Influence of the Organic Cation Layer. *Inorg. Chem.* **2000**, *39* (26), 6107−6113.

(34) Slavney, A. H.; Leppert, L.; Saldivar Valdes, A.; Bartesaghi, D.; Savenije, T. J.; Neaton, J. B.; Karunadasa, H. I. Small-Band-Gap Halide Double Perovskites. *Angew. Chem., Int. Ed.* **2018**, *57* (39), 12765−12770.

(35) Slavney, A. H.; Smaha, R. W.; Smith, I. C.; Jaffe, A.; Umeyama, D.; Karunadasa, H. I. Chemical Approaches to Addressing the Instability and Toxicity of Lead−Halide Perovskite Absorbers. *Inorg. Chem.* **2017**, *56* (1), 46−55.

(36) Shannon, R. Revised Effective Ionic Radii and Systematic Studies of Interatomic Distances in Halides and Chalcogenides. *Acta Crystallogr., Sect. A: Cryst. Phys., Diffr., Theor. Gen. Crystallogr.* **1976**, *32* (5), 751−767.

(37) Vittal, J. J.; Puddephatt, R. J. Gold: Inorganic & Coordination Chemistry. *Encyclopedia of Inorganic Chemistry* **2006**, DOI: 10.1002/0470862106.ia081.

(38) Sengodan, S.; Choi, S.; Jun, A.; Shin, T. H.; Ju, Y.-W.; Jeong, H. Y.; Shin, J.; Irvine, J. T. S.; Kim, G. Layered oxygen-deficient double perovskite as an efficient and stable anode for direct hydrocarbon solid oxide fuel cells. *Nat. Mater.* **2015**, *14*, 205.

(39) Poeppelmeier, K. R.; Leonowicz, M. E.; Longo, J. M. $CaMnO_{2.5}$ and $Ca_2MnO_{3.5}$: New oxygen-defect perovskite-type oxides. *J. Solid State Chem.* **1982**, *44* (1), 89−98.

(40) Eames, C.; Frost, J. M.; Barnes, P. R. F.; O'Regan, B. C.; Walsh, A.; Islam, M. S. Ionic transport in hybrid lead iodide perovskite solar cells. *Nat. Commun.* **2015**, *6* (1), 7497.

(41) Senocrate, A.; Maier, J. Solid-State Ionics of Hybrid Halide Perovskites. *J. Am. Chem. Soc.* **2019**, *141* (21), 8382−8396.

(42) Lindquist, K. P.; Mack, S. A.; Slavney, A. H.; Leppert, L.; Gold-Parker, A.; Stebbins, J. F.; Salleo, A.; Toney, M. F.; Neaton, J. B.; Karunadasa, H. I. Tuning the bandgap of $Cs_2AgBiBr_6$ through dilute tin alloying. *Chem. Sci.* **2019**, *10* (45), 10620−10628.

(43) Hoke, E. T.; Slotcavage, D. J.; Dohner, E. R.; Bowring, A. R.; Karunadasa, H. I.; McGehee, M. D. Reversible photo-induced trap formation in mixed-halide hybrid perovskites for photovoltaics. *Chem. Sci.* **2015**, *6* (1), 613−617.

(44) Walsh, A.; Scanlon, D. O.; Chen, S.; Gong, X. G.; Wei, S.-H. Self-Regulation Mechanism for Charged Point Defects in Hybrid Halide Perovskites. *Angew. Chem., Int. Ed.* **2015**, *54* (6), 1791−1794.

(45) Yang, T. Y.; Gregori, G.; Pellet, N.; Gratzel, M.; Maier, J. The Significance of Ion Conduction in a Hybrid Organic−Inorganic Lead-Iodide-Based Perovskite Photosensitizer. *Angew. Chem., Int. Ed.* **2015**, *54* (27), 7905−10.

(46) Kubelka, P.; Munk, F. Z. Ein Beitrag zur Optik der Farbanstriche. *Z. Technol. Phys.* **1931**, *12*, 593−601.

(47) Tanaka, K.; Takahashi, T.; Ban, T.; Kondo, T.; Uchida, K.; Miura, N. Comparative Study on the Excitons in Lead-Halide-Based Perovskite-Type Crystals $CH_3NH_3PbBr_3$ $CH_3NH_3PbI_3$. *Solid State Commun.* **2003**, *127* (9), 619−623.

(48) Heidrich, K.; Künzel, H.; Treusch, J. Optical Properties and Electronic Structure of $CsPbCl_3$ and $CsPbBr_3$. *Solid State Commun.* **1978**, *25* (11), 887−889.

(49) Liu, X. J.; Matsuda, K.; Moritomo, Y.; Nakamura, A.; Kojima, N. Electronic structure of the gold complexes $Cs_2Au_2X_6$ (X=I, Br, and Cl). *Phys. Rev. B: Condens. Matter Mater. Phys.* **1999**, *59* (12), 7925−7930.

(50) Perdew, J. P.; Burke, K.; Ernzerhof, M. Generalized Gradient Approximation Made Simple. *Phys. Rev. Lett.* **1996**, *77* (18), 3865−3868.

(51) Kresse, G.; Furthmüller, J. Efficient Iterative Schemes for Ab Initio Total-Energy Calculations Using a Plane-Wave Basis Set. *Phys. Rev. B: Condens. Matter Mater. Phys.* **1996**, *54* (16), 11169−11186.

(52) Eperon, G. E.; Hörantner, M. T.; Snaith, H. J. Metal halide perovskite tandem and multiple-junction photovoltaics. *Nat. Rev. Chem.* **2017**, *1* (12), 0095.

(53) Wolf, N. R.; Connor, B. A.; Slavney, A. H.; Karunadasa, H. I. Doubling the Stakes: The Promise of Halide Double Perovskites. *Angew. Chem., Int. Ed.* **2021**, DOI: 10.1002/anie.202016185.